Tellus
SERIES A
DYNAMIC
METEOROLOGY
AND OCEANOGRAPHY
PUBLISHED BY THE INTERNATIONAL METEOROLOGICAL INSTITUTE IN STOCKHOLM

Tellus (2011), 63A, 1028–1037

TELLUS

Simulations of the snow covered sea ice surface temperature and microwave effective temperature

By RASMUS T. TONBOE*, GORM DYBKJÆR and JACOB L. HØYER, *Danish Meteorological Institute, Lyngbyvej 100, DK-2100 Copenhagen, Denmark*

(Manuscript received 10 September 2010; in final form 26 May 2011)

ABSTRACT

The snow surface on thick multiyear sea ice in winter is on average colder than the air because of the negative radiation balance. Beneath the snow surface there is a strong temperature gradient in winter with increasing temperatures towards the ice–water interface temperature at the freezing point around –1.8 °C. The sea ice surface temperature and the thermal microwave brightness temperature were simulated using a combination of thermodynamic and microwave emission models.

The simulations indicate that the physical snow–ice interface temperature or alternatively the 6 GHz effective temperature have a good correlation with the effective temperature at the temperature sounding channels near 50 GHz. The complete correlation matrix based on the simulations for physical and effective temperatures is given.

The physical snow–ice interface temperature is related to the brightness temperature at 6 GHz vertical polarization as expected. However, the emissivity factor normally used when converting brightness temperature to the ice temperature is dependent on the ice temperature. The simulations indicate that a simple model may be used to derive the snow-ice interface temperature from satellite AMSR 6 GHz measurements.

1. Introduction

The snow surface temperature is among the most important variables in the sea ice energy balance equation and it significantly affects the atmospheric boundary layer structure, the turbulent heat exchange and the ice growth rate (Maykut, 1986). In addition, advanced thermodynamic ice models treat the temperature of the snow surface and snow–ice surface as vital parameters for the development of the sea ice in the model (e.g. Fichefet and Maqueda, 1997; Bitz and Lipscomb, 1999). Because of the large temperature gradients in the winter snow-pack, the snow surface temperature may be significantly different from the snow–ice interface temperature and the effective temperature (Hwang and Barber, 2008; Mathew et al., 2008). The effective temperature (T_{eff}, sometimes called the skin temperature), measured by microwave radiometers is an integrated temperature for a layer with a thickness, which is proportional to the penetration depth (Mathew et al., 2009). Accurate estimation of both the emissivity and the effective temperature is critical for atmospheric sounding applications over sea ice (English, 2008; Heygster et al., 2009). Further, information on both the temperature at the surface and the snow–ice interface (snow–ice temperature) from satellite observations could give important information about the vertical thermodynamics and assist in calibrating and validating the multilayer sea ice models.

Therefore it is important to describe the relationships between the temperature profile in the snow and ice, which can be simulated in models, and the brightness temperature, which can be measured by satellite infrared and microwave radiometers. In particular, this paper describes the relationship between the effective temperature near 50 GHz, with the snow and ice temperature profile and the brightness temperature at 6 GHz.

The effective temperature (T_{eff}) (K) is well defined in terms of brightness temperature (T_{b}) (K) and emissivity (e), that is

$$T_{\mathrm{eff}} = T_{\mathrm{b}}/e. \tag{1}$$

However, its link with measurable quantities in the natural snow and ice cover is not understood in detail. Therefore, the microwave emission processes from sea ice are simulated here using a one dimensional thermodynamic sea ice model with the European Centre for Medium Range Weather Forecast (ECMWF) reanalysis ERA40 input, and a microwave emission model. The focus here is on multiyear ice covered areas where the ice concentration is near 100% and where the primary variability is due to scattering, snow cover and temperature variations. The thermodynamic model does not handle extended periods of melt, therefore the summer melt period typically from June through

*Corresponding author.
e-mail: rtt@dmi.dk
DOI: 10.1111/j.1600-0870.2011.00530.x

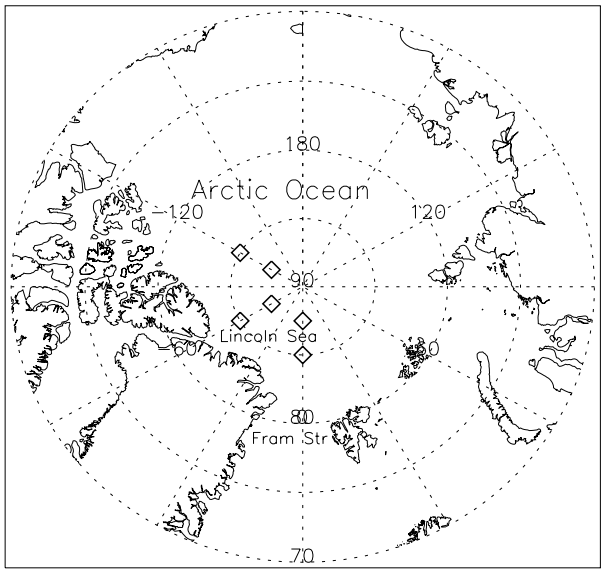

Fig. 1. The six multiyear ice profile positions with diamonds.

August is not considered here. The sea ice emission processes at microwave frequencies 6, 10, 19, 37, 50 and 89 GHz vertical and horizontal polarisation at an incidence angle of 50° are mapped. This is similar to the channels and geometry on the AMSR radiometer instruments launched on-board the ADEOS II and the AQUA satellites (the AMSR instrument on the AQUA satellite does not have temperature sounding channels near 50 GHz).

The symbol T is used for temperature. For brightness temperatures the polarisation is vertical, v, or horizontal, h and the electromagnetic frequency in GHz is denoted: T_b [frequency] [polarisation].

2. The combined thermodynamic and emission models

The ERA40 parameters used as input to the thermodynamic model are: The surface air pressure, the 2 m air temperature, the 10 m wind speed, the incoming short-wave solar radiation, the incoming long-wave radiation, the dew point temperature and precipitation. The simulations from the 1-D thermodynamic model from 1 September to 31 May are distributed at six ERA40 grid point positions covered by perennial ice. The six positions are shown in Fig. 1. The output from the thermodynamic model is used as input to the emission model.

The emission model is a sea ice version of the Microwave Emission Model for Layered Snow-packs (MEMLS) (Wiesmann and Mätzler, 1999). Sea ice dielectric and scattering functions were added to MEMLS in order to simulate the emission processes from sea ice layers beneath the snow. The modifications for the sea ice version are further described in Mätzler et al. (2006).

An example showing the penetration depth and snow depth from the profile nearest Fram Strait at 85N; 0E is illustrated in Fig. 2. The microwave's penetration is into the ice except the 89 GHz penetrating to or near the snow ice interface. Figure 3 shows the $T_{\mathrm{eff}}v$ at 6, 18, 36, 50 and 89 GHz. The coldest temperatures are for those channels with the shallowest penetration in winter. During autumn and spring the profile is nearly isothermal and the $T_{\mathrm{eff}}v$ at different frequencies are nearly equal.

Combined thermodynamic and emission models have the potential to build long time series of physical snow and sea ice temperatures as well as time series of microwave brightness temperatures that can be used for statistical analysis of radiometer and sea ice data variability (Mätzler et al., 2006; Tonboe, 2010). However, the models do not capture the spatial variability of the sea ice cover caused for example, by ice convergence resulting in deformation, ice divergence resulting in new-ice formation and wind redistribution of the snow cover affecting snow depth, density and grain size. The motion and resulting deformation of sea ice makes direct comparison between the simulations and satellite data in time and space difficult. Instead the mean simulated signatures are compared to typical AMSR multiyear sea ice signatures. This comparison reveals if the models captures the principal sea ice emissivity variability during winter. It does not provide particular reference to individual meteorological events or ice floes.

Our model set-up for snow and sea ice does not include the atmospheric emission processes. However, the data measured by satellites include atmospheric emission, which is from minimum 3 to maximum 100 K in Arctic regions for the window channels between 6 and 89 GHz.

The interface between the thermodynamic and the emission model is further described in Tonboe (2010).

2.1. The snow and sea ice emission model

Sea ice emission models relate physical snow and ice properties such as density, temperature, snow crystal and brine inclusion size to microwave attenuation, scattering and reflectivity. The model used here is a sea ice version of MEMLS (Wiesmann and Mätzler, 1999) described in Mätzler et al. (2006) and hereafter called the emission model. The theoretical improved Born approximation was used here, which validates for a wider range of frequencies and scatterer sizes than the empirical formulations (Mätzler and Wiesmann, 1999). Using the improved Born approximation the shape of the scatterers is important for the scattering magnitude (Mätzler, 1998). The snow grains grow in size as a function of snow metamorphosis after deposition. We assume spherical ice grain scatterers in snow when the correlation length, a measure of size and distribution, is less than 0.2 mm to resemble wind-slab and when it is greater than 0.2 mm the scatterers are assumed to be ice cups resembling depth hoar. The sharp transition between scatterer shapes is not occurring in natural snow packs and it is not well

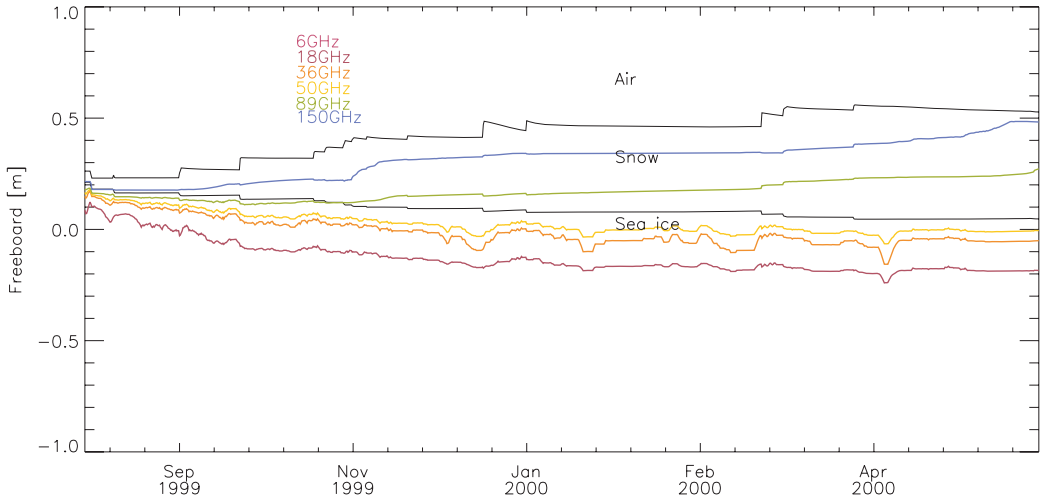

Fig. 2. The penetration depth at 6, 18, 36, 50 and 89 GHz and the snow thickness as a function of time from 1 September 1999 to 31 May 2000 at 85°N, 0°E.

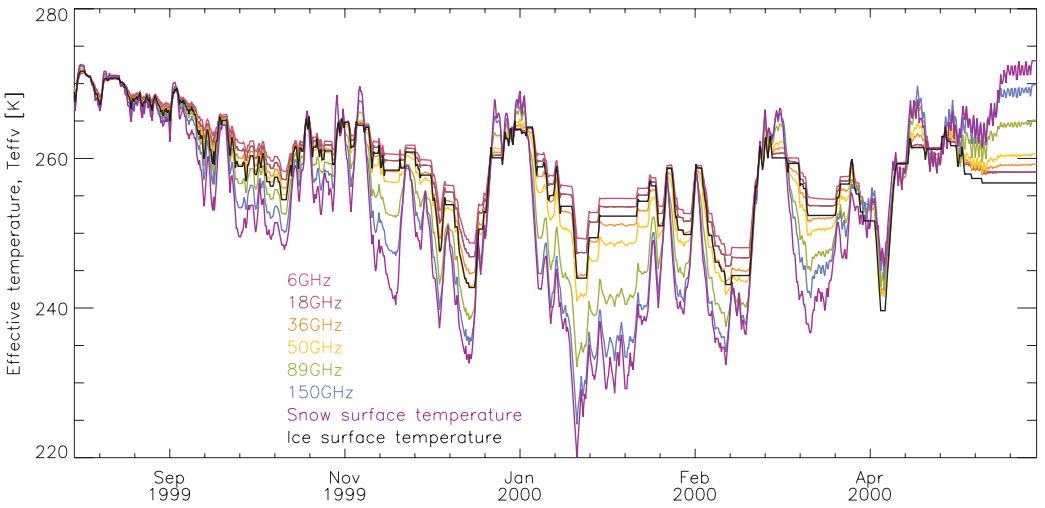

Fig. 3. The effective temperature at 6, 18, 36, 50 and 89 GHz and the snow and ice surface temperature as a function of time from 1 September 1999 to 31 May 2000 at 85°N, 0°E.

known how the different shapes coexist but the current set-up ensures that the dominating scattering mechanism and shape of scatterers in wind-slab and depth hoar are represented for each layer in the model. Scattering in the ice is caused by spherical air-bubbles. The infrared part of the spectrum is not simulated in the emission model and the snow surface temperature is assumed to be identical with the temperature measured by infrared radiometers.

2.2. *The snow and sea ice thermodynamic and mass model*

In order to produce input to the emission model a one-dimensional snow and ice thermodynamic model has been developed. Its purpose is not necessarily to reproduce a particular situation in time and space but rather to provide realistic microphysical input to the emission model.

The model computes the thermodynamic and mass state of the snow/sea ice system using the ECMWF ERA40 meteorological input data. The functions used in the model are from the open literature. The initial snow and ice profile shown in Table 1 is ordered top to bottom with the following parameters for each layer: layer number, thermometric temperature (K), type (new snow, old snow, first-year ice, multiyear ice), density (kg m^{-3}), thickness (m), scatterer correlation length (mm) (grain or inclusion size), salinity (ppt), liquid water content (m^3 m^{-3}). The meteorological data input file has the following parameters: time (decimal days), surface air pressure (hPa), air temperature (K), wind speed (m s^{-1}), incoming short-wave radiation (W m^{-2}), incoming long-wave radiation (W m^{-2}), relative humidity (%),

Table 1. The initial multiyear ice (MYI) profile input to the thermodynamic model

Number	T (K)	Type	Density (kg m^{-3})	Thickness (m)	Correlation length (mm)	Salinity (ppt)	Water content (%)
1	270	Old snow	300	0.05	0.15	0.0	0.0
2	270	MYI	900	0.05	0.35	0.5	0.0
3	270	MYI	910	0.15	0.35	1.0	0.0
4	270	MYI	910	230.0	0.25	2.5	0.0

mass of precipitation (kg m^{-2}). It has been necessary to develop certain special features in order to handle the physics of the snow and sea ice system: (1) Snow on sea ice may contain brine which is accounted for in the computation of the thermal properties, (2) For sea ice it has a growth rate dependent salinity profile.

The vertical resolution in the snow pack is determined by individual precipitation events and the subsequent metamorphosis. In the ice the resolution is 5 cm and the ice is growing at the ice–water interface. Because the thermal conductivity is a function of temperature the model uses an iterative procedure between each time step of 6 h.

The thermal properties include the thermal conductivity and the specific heat. The thermal conductivity of snow is a function of its density and temperature and sea ice its salinity and temperature. The specific heat of snow/slush/saline ice is a function of the fractions of ice and brine and its temperature if there is any brine or liquid water.

The thermal snow conductivity (W mK^{-1}), k_{snow}, is computed using Makshtas (1998), that is,

$$k_{\text{snow}} = 2.845 \times 10^{-6}\rho_{\text{snow}}^2 + 2.7 \times 10^{-4} 2^{\frac{T-233}{5}}, \tag{2}$$

where ρ_{snow} is the snow density (kg m^{-3}) and T is the snow temperature (K).

The thermal conductivity of saline ice, k_{ice}, is computed using Makshtas (1998), that is,

$$k_{\text{ice}} = 2.03 + \frac{0.12S}{T - 273.0}, \tag{3}$$

where S (ppt) is the salinity and T the ice temperature (K).

The specific heat (J kgK^{-1}) of snow, saline slush or saline ice, c, is a simplification of eq. 5.4 on p. 73 in Doronin and Kheisin (1977), that is,

$$c = c_{\text{pure ice}}\frac{M_{\text{ice}}}{M} + c_{\text{brine}}\frac{M_{\text{brine}}}{M} + L_{\text{w}}M_{\text{brine}}\frac{\partial V_{\text{brine}}}{\partial T}, \tag{4}$$

where c_{pureice} is the specific heat of pure ice (2113 J kgK^{-1}), c_{brine} is the specific heat of brine (4217 J kgK^{-1}), M_{i} is the mass of pure ice (kg), M is the total mass, M_{brine} is the mass of brine (kg), L_{w} is the latent heat of fusion (0.334×10^6 J kg^{-1}) and dV_{brine}/dT is gradient of brine volume change for a 1 K temperature change.

In the Maykut and Untersteiner (1971) 'standard case' the net short and long wave radiation balance is about neutral at the end of the year. The net long wave radiation balance is negative during summer and winter while short wave energy input is positive only during summer.

Short wave energy penetrates the snow surface and is absorbed in the snow and ice. The albedo, α, is a function of snow density, ρ_{surface} (Lefebre et al., 2003) that is,

$$\alpha = 0.58 - 4.35 \times 10^{-4}(\rho_{\text{surface}} - 920). \tag{5}$$

The multiyear ice albedo is 0.75. The snow extinction coefficient, γ_{e}, is set according to snow density, ρ_{s} and snow grain size diameter, x_{gs}, (Jordan et al., 1999) that is,

$$\gamma_e = 3.795 \times 10^{-3}\frac{\rho_s}{\sqrt{x_{gs}}}. \tag{6}$$

The multiyear ice extinction coefficient is 2.5. The deposit of shortwave energy in each layer of thickness z, is the difference between energy (J) at the top (Q_{a}) and at the bottom (Q_{b}) of the layer, that is,

$$Q_b = Q_a e^{\frac{-\gamma_e}{z}}. \tag{7}$$

The long-wave energy balance at the surface is the difference between emitted and absorbed incoming radiation, that is,

$$Q_{\text{lw}} = e_{\text{s}}Q_{\text{il}} - e_{\text{s}}k_{\text{b}}T_{\text{s}}^4, \tag{8}$$

where e_{s} is the surface emissivity (0.98), Q_{il} the incoming long wave radiation, k_{b} is Stephan Boltzmans constant (5.67051×10^{-8} W m^{-3}K^{-4}) and T_{s} is the surface temperature (K).

The latent, sensible and precipitation heat fluxes exchange heat between the surface and the atmosphere. The conductive heat flux exchange heat within the snow and ice.

Latent heat is the energy added to the surface by condensation of water vapour or removed by evaporation. The magnitude of latent heat loss is greater during summer than winter (Maykut and Untersteiner, 1971).

Sensible heat, Q_{sensible}, is the energy added or removed from the surface by momentum fluxes in the lowest atmosphere. The net Q_{sensible} is negative during summer and positive during winter (Maykut and Untersteiner, 1971).

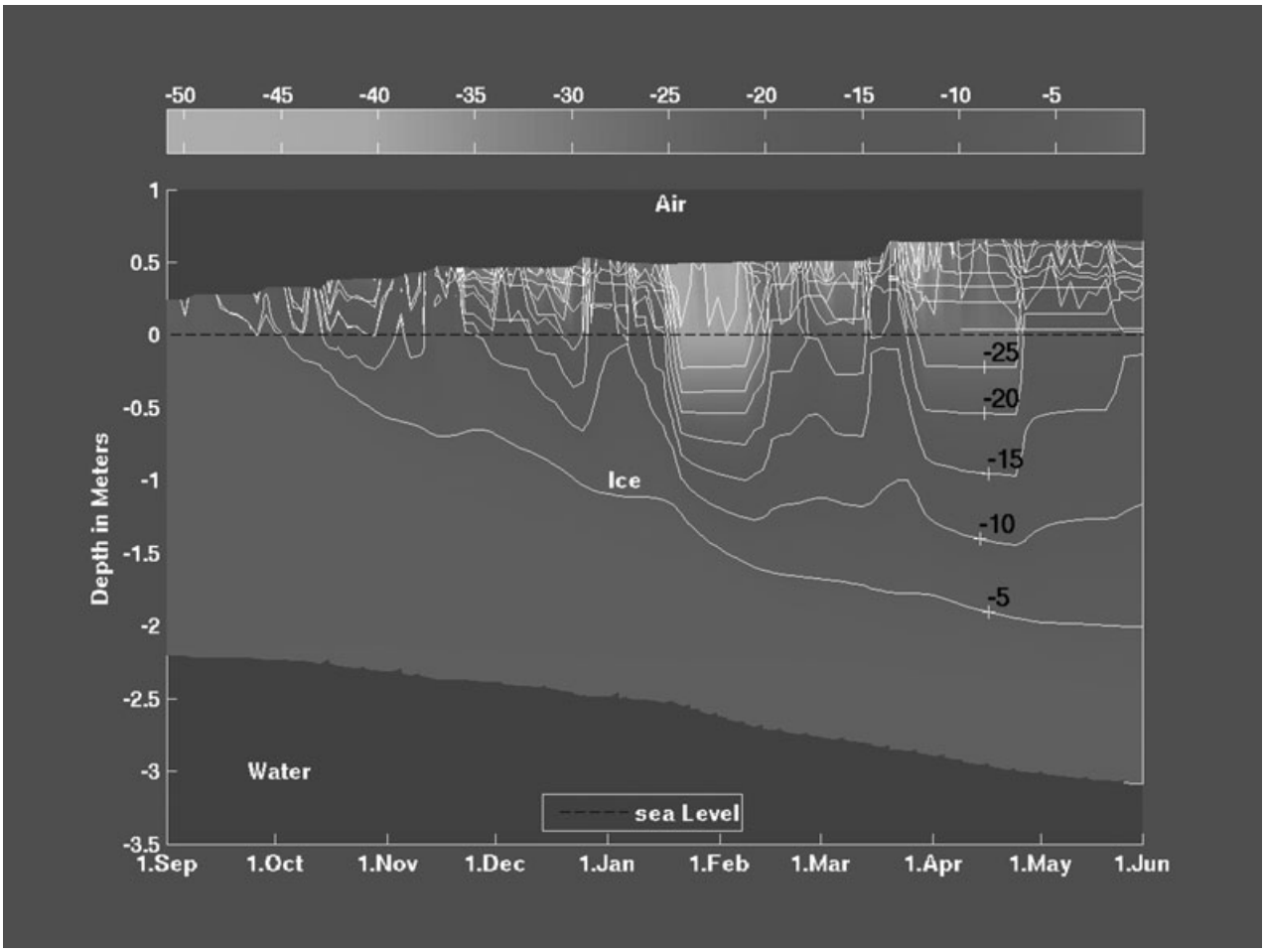

Fig. 4. The profile temperature (°C) and snow/ice thickness (m) as a function of time from 1 September 1999 to 31 May 2000 at 85°N, 0°E.

The conductive heat flux is simply the thermal conductivity, k, times the temperature gradient, that is,

$$Q_{\text{conductive}} = k\frac{\partial T}{\partial z}. \tag{9}$$

The ice thickness is increasing during winter in response to the negative energy budget (thermodynamic growth). The growth rate is proportional to the energy budget of the bottom layer. Its salinity (ppt), S, is a function of growth rate, dz/dt, (Nakawo and Sinha, 1981), that is,

$$S = 32.0\frac{0.12}{0.12 + 0.88\text{e}^{-4.2\times10^4}\dfrac{\partial z}{\partial t}}. \tag{10}$$

The compaction is computed using (a corrected version of) Brun et al. (1989). The snow compaction rate is a function of the snow load F_{snow} (N m^{-2}), density ρ_{snow} (kg m^{-3}) and temperature (K), T, that is,

$$z = \left(1 - F_{\text{snow}}\frac{t}{a}\right)z, \tag{11}$$

where

$$a = 10.0 \times 10^4\text{e}^{23.0\rho_{\text{snow}} - 0.1(T - T_{\text{melt}})}. \tag{12}$$

The density (kg m^{-3}), ρ_{snow}, of added snow layers is a function of air temperature (K), T_{air} and wind speed (m s^{-1}), u, (Jordan et al., 1999), that is,
if $T_{\text{air}} > 260.15$ K,

$$\rho_{snow} = 500\left(1.0 - 0.951\text{e}^{-1.4(278.15 - T_{\text{air}})^{-1.15}} - 0.008u^{1.7}\right) \tag{13}$$

else,

$$\rho_{\text{snow}} = 500\left(1.0 - 0.904\text{e}^{-0.008u^{1.7}}\right). \tag{14}$$

The snow density, ρ_{snow}, due to metamorphosis is computed using Sturm and Holmgren (1998), that is,

$$\rho_{\text{snow}} = \rho_{\text{snow}} + \frac{F_{\text{snow}}\rho_{\text{snow}}t}{\mu_o\text{e}^{k\rho_{\text{snow}}}}, \tag{15}$$

where $k = 0.02$ is a constant, $\mu_0 = 8.5 \times 10^6$ is the snow viscosity (Ns m^{-2}). The metamorphosis of snow grains in the model is described in Tonboe (2005 and 2010).

2.3. Model set-up

Climatology indicates that there is snow on multiyear ice at the end of summer melt in September (Warren et al., 1999). Therefore, the multiyear ice simulations are initiated on 1 September with an isothermal 2.5 m ice floe at 270 K with a 5 cm old snow layer on top. The initial profile is shown in Table 1. Meteorological records from six different ERA40 grid points between latitudes 85 and 87.5°N and longitudes 0 and 120°W in a region between North Greenland and the North Pole are used as input to the thermodynamic model. The profile positions are shown in Fig. 1.

The multiyear ice gradually grows at these six positions from 2.5 m to between 3.0 m and 3.4 m in spring and snow depths during winter range between 0.2 m and 0.5 m. The temperature distribution in the snow and ice as a function of time is shown for the profile nearest Fram Strait at 85°N, 0°E in Fig. 4. The profile in Fig. 4 has 50 ice layers and 1 snow layer at the beginning of the simulation and there are 62 ice layers and 30 snow layers at the end of the simulation. The melt processes during the summer season are complicated and not sufficiently described by the thermodynamic model. Summer melt is therefore not included in this study and the simulations end on May 31. The data from all six profile-positions comprise observations between 1 September 1999 and 31 May 2000 with data points every 6 h.

2.4. Model comparison to measurements

The gradient ratio (*GR1937*) is the difference over the sum of *Tb37v* and *Tb19v* and the polarisation ratio (*PR19*) is the difference over the sum of *Tb19v* and *Tb19h* (Comiso et al., 1997). The NASA Team ice concentration algorithm is computing the ice concentration in *PR19* and *GR1937* space using typical signatures for open water, first-year ice and multiyear ice called tie-points. The simulations between December and May are shown in Fig. 5 together with the tie-points for multiyear ice, first-year ice and open water. A sample AMSR data set from December 2002 to May 2003 is included in the plot for comparison. The sample AMSR data are the daily means of 80 pixels (25 × 25 km^2 pixel size) in the region of interest North of Greenland covered nearly exclusively by multiyear ice. Both the negative gradient and the polarisation ratio of the simulations are slightly overestimated compared to the tie-points. However, there is a large overlap between the simulations and the measured sample and the cluster of simulated signatures is near the 100% ice concentration line between the first and multiyear ice tie-points. The small difference between the cluster of simulated and measured data points cannot be explained by atmospheric emission included in the satellite measurements and not included in the model. Cloud liquid water and water vapour in the atmosphere reduces both *GR1937* and *PR19* (Oelke, 1997). Instead, we speculate that the differences are due to physical processes not described in the thermodynamic model such as ice deformation

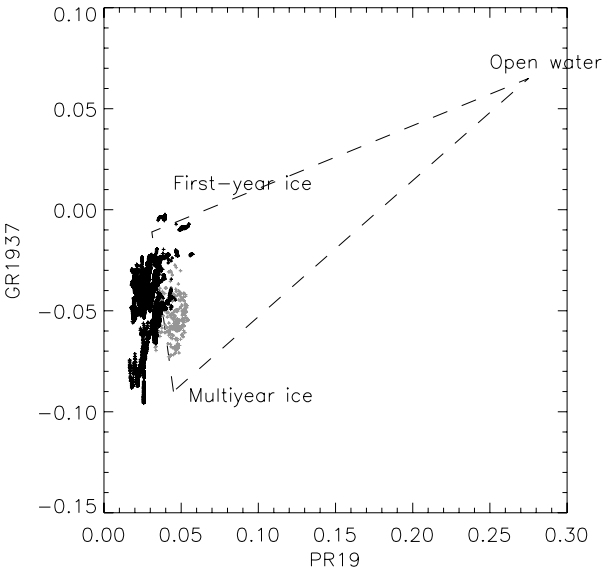

Fig. 5. Simulated multiyear ice *GR1937* and *PR19* (black points) compared to typical first-year ice, multiyear ice and open water signatures (the NASA team tie-points). AMSR satellite data are included for comparison (grey points).

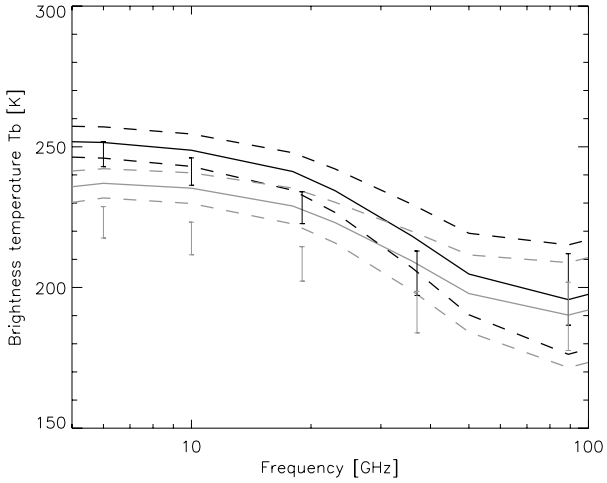

Fig. 6. Simulated *Tbv* (black) and *Tbh* (grey) between 5 and 100 GHz compared to measured *Tb* at 6, 10, 19, 37 and 89 GHz from AMSR-E Arctic Ocean multiyear ice. The dashed lines show ± one standard deviation around the mean of simulated data.

including divergence and convergence and wind redistribution of the snow cover scouring and carving the metamorphosed parts of the snow-pack.

Figure 6 shows the mean simulated T_b with continuous lines (±one standard deviation with dashed lines) and the mean T_b (±one standard deviation) from the sample AMSR data set between 5 and 100 GHz. The initial three months September–November are excluded from the comparison. There is an overlap between measured and simulated *GR1836* and *PR18* as seen in Fig. 5. It is noted that there is overlap between

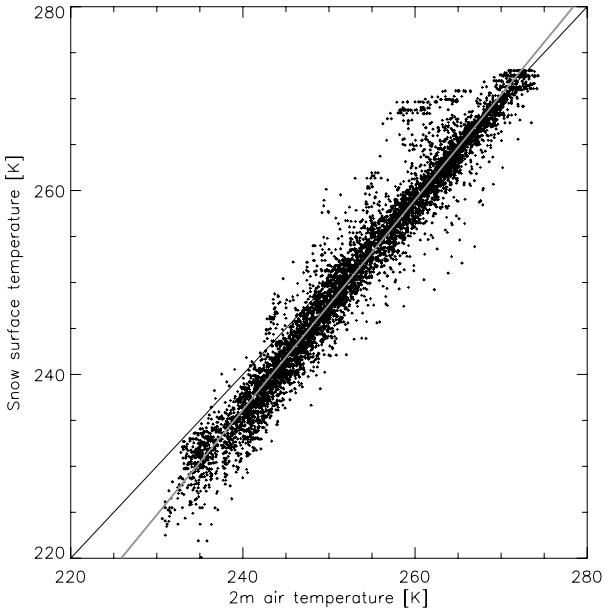

Fig. 7. The 2-m air temperature versus the simulated snow surface temperature. The best fit line shown in grey is $T_{\text{snow}} = 1.14 * T_{\text{air}} - 37.94$.

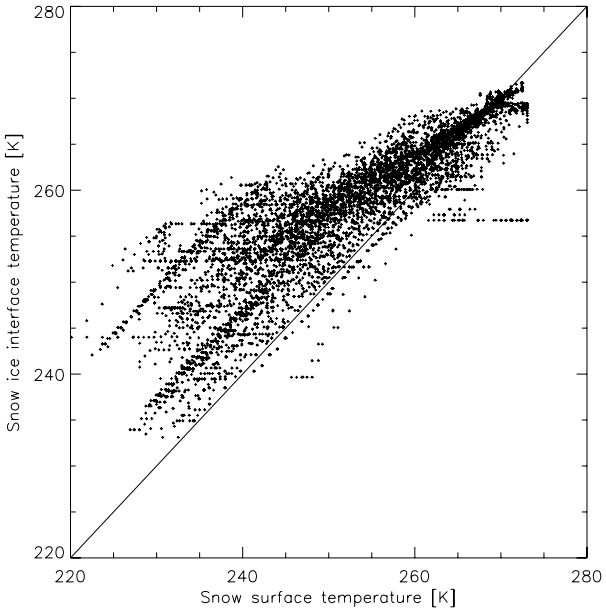

Fig. 8. The simulated snow surface temperature versus the snow–ice interface temperature for multiyear ice.

simulated and measured $T_b v$. However, the simulated mean $T_b v$ and $T_b h$ are higher than the measured sample data. The initial profile T_b in the beginning of the simulation is close to a typical first-year ice T_b, which means that the T_b is high compared to typical multiyear ice T_b in particular at 10, 19 and 37 GHz. The simulated T_b remains high during the winter because of its initial high level even though snow gradually accumulates and scattering in the snow decreases the emissivity and the T_b. This is the reason for excluding the first 3 months from the AMSR data comparison. The summer melt processes cannot be simulated here to produce a more realistic initial profile and the current set-up is therefore retained.

3. Emitting temperature simulation results and discussion

The atmospheric boundary layer over thick ice in winter when it is dark in winter is stable and there is a positive sensible heat flux from the air to the surface to compensate the negative (longwave) radiation budget. The surface is on average colder than the air (Maykut, 1986). This is corroborated in Fig. 7, where the 2 m air temperature versus the simulated snow surface temperature show a cold bias at the coldest winter temperatures.

3.1. The temperature profile

Through the snow layer, from the cold snow surface to the warmer snow–ice interface, the simulations show that there is a steep temperature gradient of 27 K m^{-1} on average during winter. The mean snow depth is 0.26 m. The temperature gradient standard deviation is 25 K m^{-1}. The temperature gradient in multiyear ice is 5 K m^{-1} for comparison. The multiyear ice is 2.8 m thick on average. Figure 8 shows the simulated snow surface temperature versus the snow–ice interface temperature. As expected, when temperatures are warm near 270 K then the differences between the snow surface and the snow–ice interface temperature are relatively small. At colder temperatures the differences can be up to 20 K.

3.2. Brightness temperature

The microwave's penetration into the snow and sea ice is a function of attenuation and scattering. The attenuation in the snow is a function of the imaginary part of the dielectric constant, for the snow or ice sometimes called the loss. The loss is an order of magnitude larger for liquid water than for ice. This means that melt-water in the snow or liquid brine-pockets in the saline ice effectively block further penetration. The loss of melt water and saline brine is nearly the same for frequencies higher than about 10 GHz (Ulaby et al., 1986). The scattering is a function of frequency, the scatterer size and the permittivity contrast between the scatterer and the background (Mätzler, 1998) and the extinction is the sum of the attenuation and the scattering. The extinction in snow and ice is higher for higher frequencies primarily because of scattering. The penetration into the snow and ice is therefore deeper at 6 GHz than at 89 GHz. The effective temperature is the integrated emitting layer temperature. At 6 GHz the penetration into the saline ice, that is, the penetration depth, is a function of the ice temperature. This means

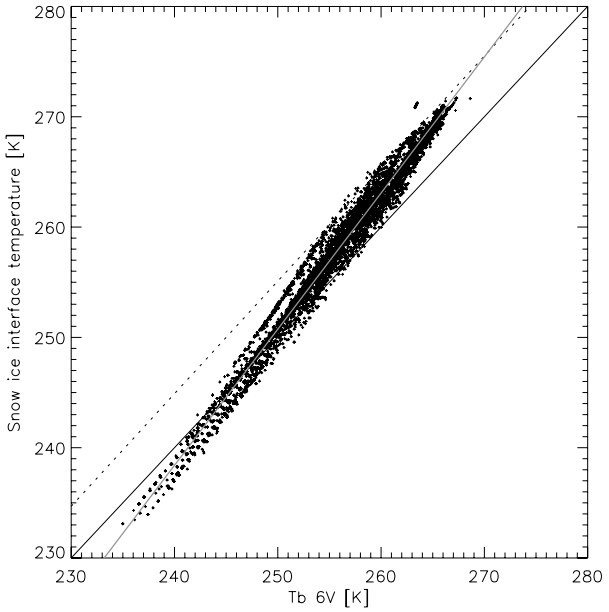

Fig. 9. The T_b6v versus the multiyear ice snow–ice interface temperature. The dashed line shows the $T_b6v = 0.98{*}T_{\text{eff}}6v$ which is a common model for deriving ice temperature from 6 GHz brightness temperatures. The best fit line in grey is $T_{\text{ice}} = 1.23{*}T_b6v - 57.81$.

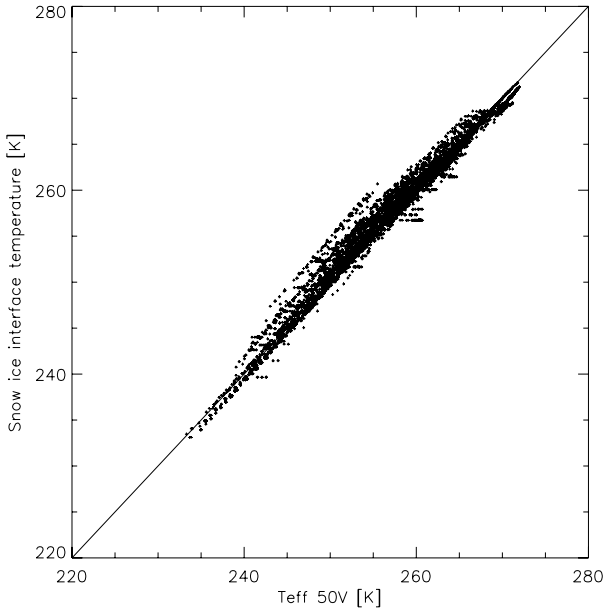

Fig. 10. The multiyear ice snow–ice interface temperature versus the effective temperature at 50 GHz ($T_{\text{eff}}50v$).

that the penetration is deeper at colder temperatures and shallower at warmer temperatures. This means the $T_{\text{eff}}6v$ is relatively warmer than the snow–ice interface temperature at colder physical temperatures because of deeper penetration as illustrated in Fig. 9. The grey line in Fig. 9 is a simple model for deriving the snow–ice interface temperature (T_{ice}) from T_b6v that is,

$$T_{\text{ice}} = 1.23 * T_b6_v - 57.81. \quad (16)$$

At higher frequencies than at 6 GHz the penetration is shallower. Figure 10 shows the snow–ice interface temperature versus the $T_{\text{eff}}50v$. Because the penetration at 50 GHz into the ice is limited there is no temperature dependence as in Fig. 9.

The simulated $T_{\text{eff}}v$ correlation matrix for multiyear ice is shown in Table 2. The correlation coefficients for the different effective temperatures are high. Also the correlations between the snow–ice interface temperature and T_{eff} between 6 and 89 GHz are high ($R > 0.95$). The snow surface temperature is relatively poorly correlated to all other temperatures except the air temperature in the matrix ($0.78 < R < 0.95$). Its highest correlation is with the $T_{\text{eff}}89v$ ($R = 0.95$). The T_{eff} is difficult to derive in practise at higher frequencies (frequency greater than 6 GHz) because of the variable surface emissivity (Tonboe, 2010). However, the simulated emissivity at 6 GHz is very stable. The mean emissivity is 0.986 with a standard deviation of only 0.0025. Because of the low 6 GHz emissivity variability it is common practise to derive the ice temperature using a simple

Table 2. The $T_{\text{eff}}v$ correlation matrix

	T_{air}	T_{snow}	T_{ice}	$T_{\text{eff}}6v$	$T_{\text{eff}}10v$	$T_{\text{eff}}18v$	$T_{\text{eff}}23v$	$T_{\text{eff}}36v$	$T_{\text{eff}}50v$	$T_{\text{eff}}89v$
T_{air}	1	0.97	0.78	0.75	0.76	0.77	0.78	0.80	0.84	0.91
T_{snow}	0.97	1	0.81	0.78	0.79	0.80	0.81	0.84	0.88	0.95
T_{ice}	0.78	0.81	1	0.99	0.99	0.99	0.99	0.99	0.98	0.95
$T_{\text{eff}}6v$	0.75	0.78	0.99	1	0.99	0.99	0.99	0.99	0.98	0.92
$T_{\text{eff}}10v$	0.76	0.79	0.99	0.9	1	0.99	0.99	0.99	0.98	0.92
$T_{\text{eff}}18v$	0.77	0.80	0.99	0.99	0.99	1	0.99	0.99	0.98	0.93
$T_{\text{eff}}23v$	0.78	0.81	0.99	0.99	0.99	0.99	1	0.99	0.99	0.93
$T_{\text{eff}}36v$	0.80	0.84	0.99	0.99	0.99	0.99	0.99	1	0.99	0.95
$T_{\text{eff}}50v$	0.84	0.88	0.98	0.98	0.98	0.98	0.99	0.99	1	0.97
$T_{\text{eff}}89v$	0.91	0.95	0.95	0.92	0.92	0.93	0.93	0.95	0.97	1

Note: The 2-m air (T_{air}), the physical snow surface (T_{snow}) and the snow–ice interface (T_{ice}) temperatures are included.

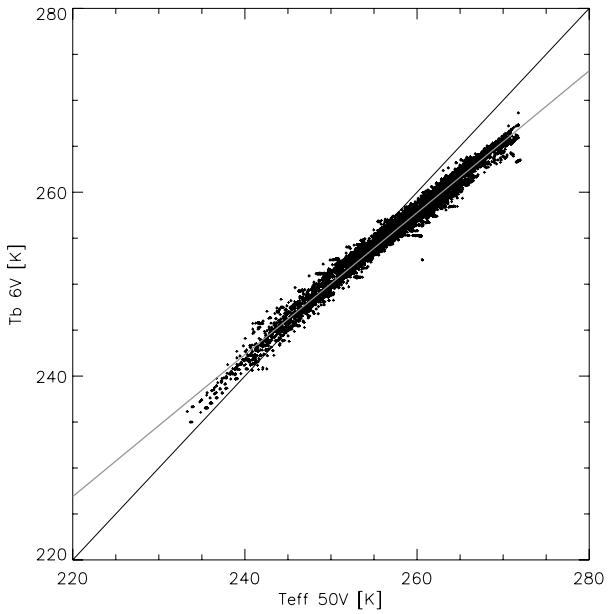

Fig. 11. The multiyear ice $T_{\text{eff}}50v$ versus the $T_{\text{b}}6v$. The best fit line in grey is $T_{\text{b}}6v = 0.77{*}T_{\text{eff}}50v + 57.06$.

model with the emissivity constrained to 0.98 (Hwang and Barber, 2008). This temperature is relatively well correlated with effective temperatures between 6 and 89 GHz as can be seen in Table 2. Figure 11 shows the $T_{\text{eff}}50v$ versus the $T_{\text{b}}6v$. The dynamic range of the $T_{\text{eff}}50v$ is greater than that of the $T_{\text{b}}6v$ but a simple model can relate the two temperatures.

The snow surface temperature and the air temperatures are prognostic variables in numerical weather prediction models. However, these model variables are poorly correlated with snow–ice interface temperature or the $T_{\text{eff}}6v$ or $T_{\text{eff}}50v$. For atmospheric temperature sounding applications in the troposphere over sea ice the $T_{\text{b}}6v$, which is measured by satellite or the $T_{\text{eff}}6v$ is a closer proxy for the $T_{\text{eff}}50v$ than the snow surface temperature is.

4. Conclusions

The relationship between the physical temperature of the snow and ice and the effective temperature is difficult to measure in the field. However, the snow surface temperature can be measured with infrared radiometers and the effective temperature at 6 GHz can be estimated using the 6 GHz brightness temperature. The snow surface temperature is affected by the variable atmospheric and radiative forcing and the snow has a low heat conduction rate. This means that there is a large temperature gradient in the snow and the ice and the surface temperature is relatively poorly correlated with both the snow–ice interface temperature and the effective temperatures between 6 and 89 GHz. However, the effective temperatures between 6 GHz and 89 GHz are highly correlated.

The simulations indicate that the 6 GHz brightness temperature can be related to the snow–ice interface temperature correcting for the temperature dependent penetration depth in saline ice. The penetration is deeper at colder air temperatures and shallower at warmer air temperatures. This means the $T_{\text{eff}}6v$ is relatively warmer than the snow–ice interface temperature at colder physical temperatures because of deeper penetration. Therefore it may be possible to derive the snow–ice interface temperature from the 6 GHz brightness temperature. The estimated snow–ice interface temperature may be more easily used in physical modelling than the effective temperature. Hydrodynamic ocean and sea ice models with advanced sea ice modules simulate the snow surface and snow–ice temperature explicitly. The work presented here could help towards constraining the vertical thermodynamics in the models for large areas, such as the Arctic sea ice cover during winter.

Both the near 50 GHz emissivity and the effective temperature are needed for atmospheric temperature sounding application over sea ice. The simulations with the combined thermodynamic and emission model show that the 6 GHz brightness or effective temperature estimates (Hwang and Barber, 2008) or the snow–ice interface temperature is a closer proxy for the effective temperature near 50 GHz than the snow surface temperature.

It was demonstrated in this study that simulated and measured winter multiyear ice T_{b} and its variability in the 6 to 89 GHz range are comparable. Further validation of the emission model requires coincident infrared and microwave radiometer measurements and snow and ice measurements in the field. The field measurements that would be needed for validation of the model include the snow and ice temperature. The most important temperature measurements are at the snow surface and the snow–ice interface. Other measurements include the snow and ice thickness and its spatial variability. The microphysical measurements include snow and ice density, snow grain sizes, snow and ice stratigraphy, snow liquid water content and snow and ice salinity.

5. Acknowledgment

We are grateful for the constructive comments from two anonymous reviewers. The meteorological input data to the thermodynamic model were provided by the ECMWF. The layout of Fig. 4 was prepared by Jon Saabye. This work was funded by the EU FP6 project Damocles and the Danish Agency for Science, Technology and Innovation and is a part of the Greenland Climate Research Centre.

References

Bitz, C. and Lipscomb, W. 1999. An energy-conserving thermodynamic model of sea ice. *J. Geophys. Res.* **104**(C7), 15 669–15 677.

Brun, E., Martin, E., Simon, V., Gendre, C. and Coleou, C. 1989. An energy and mass model of snow cover suitable for operational avalanche forecasting. *J. Glaciol.* **35**(121), 333–342.

Comiso, J. C, Cavalieri, D. J., Parkinson, C. L. and Gloersen, P. 1997. Passive microwave algorithms for sea ice concentration: a comparison of two techniques. *Remote Sens. Environ.* **60**, 357–384.

Doronin, Y. P. and Kheisin, D. E. 1977. *Sea Ice*. Amerind Publishing Co. Pvt. Ltd., New Delhi.

English, S. J. 1999. Estimation of temperature and humidity profile information from microwave radiances over different surface types. *J. Appl. Meteorol.* **38**, 1526–1527.

Fichefet, T. and Maqueda, M. A. M. 1997. Sensitivity of a global sea ice model to the treatment of ice thermodynamics and dynamics. *J. Geophys. Res.* **102**(C6), 12 609–12 646, doi:10.1029/97JC00480.

Heygster, G., Melsheimer, C., Mathew, N., Toudal, L., Saldo, R. and co-authors. 2009. POLAR PROGRAM: Integrated Observation and Modeling of the arctic Sea Ice and Atmosphere. *Bull. Am. Meteorol. Soc.* **90**, 293–297.

Hwang, B. J. and D. G. Barber. 2008. On the impact of ice emissivity on the sea ice temperature retrieval using passive microwave radiance data. *IEEE Geosci. Remote Sens. Lett.* **5**(3), 448–452.

Jordan, R., Andreas, E. and Makshtas, A. 1999. Heat budget of snow covered sea ice at North Pole 4. *J. Geophys. Res.* **104**(C4), 7785–7806.

Lefebre, F., Gallee, H., van Ypersele, J. and Greuell, W. 2003. Modeling of snow and ice melt at ETH-camp (west Greenland): a study of surface albedo. *J. Geophys. Res.* **108**(D8), 4231, doi:10.1029/2001JD001160.

Makshtas, A. P. 1998. Thermodynamics of sea ice. In: *Physics of Ice-Covered Seas*. (ed. Leppäranta, M.). University Printing House, Helsinki, 289–304.

Mathew, N., Heygster, G. and Melsheimer, C. 2009. Surface emissivity of the Arctic sea ice at AMSR-E frequencies. *IEEE Trans. Geosci. Remote Sens.* **47**(12), 4115–4124, doi:10.1109/TGRS.2009.2023667.

Mathew, N., Heygster, G., Melsheimer, C. and Kaleschke, L. 2008. Surface emissivity of polar regions at AMSU window frequencies. *IEEE Trans. Geosci. Remote Sens.* **46**(8), 2298–2306, doi:10.1109/TGRS.2008.916630.

Mätzler, C. 1998. Improved Born approximation for scattering of radiation in a granular medium. *J. Appl. Phys.* **83**(11), 6111–6117.

Mätzler, C. and Wiesmann, A. 1999. Extension of the Microwave Emission Model of Layered Snowpacks to coarse-grained snow. *Remote Sens. Environ.* **70**, 317–325.

Mätzler, C., Rosenkranz, P.W., Battaglia, A. and Wigneron, J.P., eds. 2006. *Thermal Microwave Radiation—Applications for Remote Sensing*, IEE Electromagnetic Waves Series. London, UK.

Maykut, G. A. 1986. The surface heat and mass balance. In: *The Geophysics of Sea Ice*. (ed. Untersteiner N.). NATO ASI Series, Plenum Press, New York and London, 395–464.

Maykut, G. A. and Untersteiner, N. 1971. Some results from a time-dependent thermodynamic model of sea ice. *J. Geophys. Res.* **76**(6), 1550–1575.

Nakawo, M. and N. K. Sinha. 1981. Growth rate and salinity profile of first-year sea ice in the high Arctic. *J. Glaciol.* **27**(96), 315–330.

Oelke, C. 1997. Atmospheric signatures in sea-ice concentration estimates from passive microwaves: modelled and observed. *Int. J. Remote Sens.* **18**(5), 1113–1136.

Sturm, M. and Holmgren, J. 1998. Difference in compaction behaviour of three climate classes of snow. *Ann. Glaciol.* **26**, 125–130.

Tonboe, R. T. 2005. A mass and thermodynamic model for sea ice. Danish Meteorological Institute Scientific Report 05-10, Copenhagen.

Tonboe, R. T. 2010. The simulated sea ice thermal microwave emission at window and sounding frequencies. *Tellus* **62A**, 333–344.

Ulaby, F. T., Moore, R. K., Fung, A. K. 1986. *Microwave Remote Sensing, Active and Passive*, Volume 3. Artech House, Norwood MA.

Warren, S. G., Rigor, I. G., Untersteiner, N., Radionov, V. F., Bryazgin, N. N. and co-authors. 1999. Snow depth on Arctic sea ice. *J. Clim.* **12**, 1814–1829.

Wiesmann, A. and Mätzler, C. 1999. Microwave emission model of layered snowpacks. *Remote Sens. Environ.* **70**, 307–316.